AGU PUBLICATIONS

Radio Science

RESEARCH ARTICLE
10.1002/2015RS005793

Key Points:
- Wideband multiantenna measurements are taken for high-speed railway station channels
- Large- and small-scale fading of high-speed railway station channels are characterized
- Stationary region of high-speed railway station channels is characterized

Correspondence to:
T. Zhou,
taozhou.china@gmail.com

Citation:
Zhou, T., C. Tao, S. Salous, L. Liu, and Z. Tan (2015), Channel characterization in high-speed railway station environments at 1.89 GHz, *Radio Sci.*, *50*, 1176–1186, doi:10.1002/2015RS005793.

Received 7 AUG 2015
Accepted 27 OCT 2015
Accepted article online 30 OCT 2015
Published online 24 NOV 2015

Channel characterization in high-speed railway station environments at 1.89 GHz

Tao Zhou[1], Cheng Tao[1,2], Sana Salous[3], Liu Liu[1], and Zhenhui Tan[1]

[1]Institute of Broadband Wireless Mobile Communications, Beijing Jiaotong University, Beijing, China, [2]National Mobile Communications Research Laboratory, Southeast University, Nanjing, China, [3]School of Engineering and Computing Sciences, Durham University, Durham, UK

Abstract Channel characterization is the prerequisite condition for the research and development of the next-generation high-speed railway (HSR) communication system. Train station is one of typical HSR scenarios, where channel characteristics have not yet been investigated sufficiently. In this paper, wideband multiantenna channel measurements are performed at 1.89 GHz in an open-type train station environment based on long-term evolution networks along Beijing to Tianjin HSR in China. Large-scale characteristics of the HSR station channel, focusing on path loss, shadow fading (SF), and the autocorrelation property of SF, are studied. Moreover, small-scale characteristics, such as Ricean K-factor, delay spread, and spatial correlation, are analyzed and modeled. In addition, the stationary region is characterized using the RUN test method. The obtained results provide useful information for deployment and assessment of the future HSR communication system in the HSR station scenario.

1. Introduction

In the past decade, the fast and tremendous development of high-speed railway (HSR) has promoted increasing demands for train-ground wireless communication services. The HSR services can be classified into professional services and public services. The professional services are commonly referred to as mission critical services and include critical railway communications, train operational voice services, and operational data applications [*Calle-Sanchez et al*., 2012], whereas the public services involve passenger experience services and all the business process support services such as voice and data train crew communications and train support applications. The existing railway radio systems like global system for mobile communications for railway (GSM-R) can merely provide the vital mobile voice and data communications for train drivers and track side workers. In fact, the next-generation HSR communication system aims at supporting the both kinds of HSR services simultaneously [*Ai et al*., 2014; *Zhang et al*., 2010].

Accurate characterization of the radio channel in realistic environments is the basis for the design of the wireless communication system [*Razavi-Ghods and Salous*, 2009]. So far, a few works relevant to the HSR channel characterization have been published and attracted intensive attention. For the most typical viaduct and cutting scenarios, *He et al*. [2011a, 2011b, 2013a, 2013b] carried out a series of measurements at 930 MHz based on GSM-R networks in China. Due to the large amount of experimental data, empirical models taking viaduct height, base station (BS) height, and cutting width into account were innovatively proposed for narrowband characteristics. Further, Propsound wideband measurements at 2.35 GHz in China were reported in *Liu et al*. [2012], *Guo et al*. [2012], and *Sun et al*. [2013], and both large-scale and small-scale fading were characterized. For the hilly terrain scenario, *Luan et al*. [2013] presented the large-scale fading characteristics derived by the noncommercial sounder measurements at 2.4 GHz, whereas the delay spread (DS) and Doppler characteristics were analyzed in *Zhang et al*. [2014]. A set of measurements for distributed antenna systems were conducted in the tunnel scenario on HSR in Spain, and the effects of tunnel propagation were modeled [*Briso et al*., 2007]. *Guan et al*. [2014] performed extensive 930 MHz measurements on train stations of HSR in China. The narrowband characteristics, including extra path loss (PL), shadow fading (SF), small-scale fading, level crossing rate, average fade duration, and fading depth, have been investigated.

Although channel characteristics in most HSR scenarios have already been systematically researched, there are still huge gaps on the wideband properties of the HSR station channel. Moreover, in the station environment the multiantenna measurements have not yet been carried out, and the result of the spatial feature is lacking. Apart from that, the nonstationary characteristic, which has been widely studied in vehicle-to-vehicle channels

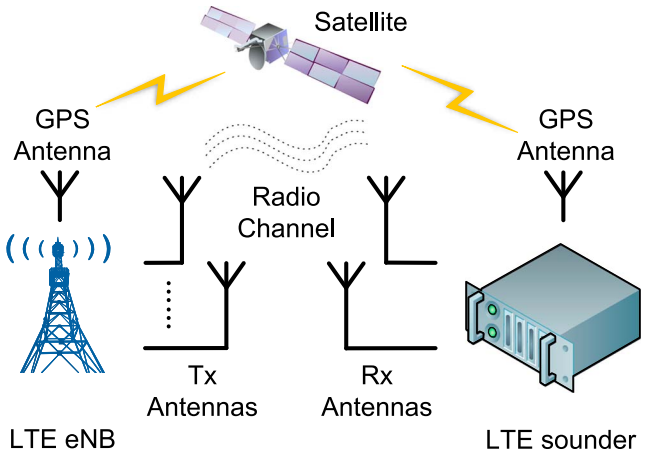

Figure 1. LTE-based channel measurement system.

[*Renaudin et al*., 2010; *Matolak*, 2014], is rarely investigated in HSR channels, especially in the station channel. In *Liu et al*. [2014], nonstationary properties based on Markov chains were provided to characterize the wireless propagation mechanism in viaduct scenarios. However, the characterization of the stationary region is not mentioned.

In this contribution, the wideband multiantenna channel measurement in a typical HSR station was first conducted at 1.89 GHz. The system used in the measurement is composed of an existing long-term evolution (LTE) eNodeB (eNB) on Beijing to Tianjin HSR in China and a custom-designed two-antenna LTE sounder that is utilized to collect the LTE signal for extracting the channel data. According to the acquired channel impulse responses (CIRs), some critical large-scale characteristics such as PL and SF and small-scale characteristics involving Ricean K-factor, DS, and spatial correlation (SC) are computed and analyzed. In addition, employing the RUN test method, the characterization of the stationary region is discussed.

2. LTE-Based Channel Measurement

2.1. Measurement System

In *Zhou et al*. [2013] and *Zhou et al*. [2015], a high-efficiency channel sounding scheme that employs the cell-specific reference signal (CRS) of LTE as the excitation signal has been proposed. The CRS, as an essential component of the LTE signal, is commonly used for channel estimation in the downlink. When it comes to the channel measurement, the CRS can be regarded as a kind of probing waveforms, whose signal structure completely determines the measurement capability. It has evaluated that the CRS, with 18 MHz measurement bandwidth (corresponding to about 56 ns time delay resolution), 11 μs time delay window, and 1 kHz maximum expected Doppler shift, is able to meet the requirements of channel measurement in HSR scenarios.

To apply this scheme in realistic measurements, a LTE-based channel measurement system is proposed, as shown in Figure 1. Both LTE eNB and LTE sounder adopt the satellite-based solution, e.g., GPS, to achieve the synchronization, which can guarantee the frequency consistency in the measurement system. Since there are four antenna ports carrying orthogonal CRSs in LTE specification, the LTE eNB can equip with up to four antennas to send out the parallel CRSs. In this system, two antennas are configured at the LTE sounder side to implement the multiantenna channel measurement.

Unlike the traditional channel sounders, the LTE sounder has only one receiver whose components are summarized in the functional block diagram of Figure 2. Full parallel architecture that receives the excitation signal simultaneously from all antennas is employed. Synchronization of the clock signals is achieved by use of the GPS frequency reference. After band-pass filtering, the resulting radio frequency (RF) signals are converted to 70 MHz intermediate frequency (IF) signals. Then, the IF signals are sampled using the analog to digital (A/D) converters (ADCs) that operate at 56 MSPS for meeting the requirement of band-pass sampling in the case of 70 MHz IF and 20 MHz bandwidth. After A/D conversion, the digitized IF signal transmission is controlled by the field-programmable gate array (FPGA) which applies the synchronous dynamic random access memory (SDRAM) to bridge data streams between the PC and the ADC. Digital signal samples are buffered in the SDRAM and then delivered into the PC memory. Finally, the collected IF data and navigation data are stored together in the solid state disk (SSD). As for postprocessing, frame and slot synchronization is implemented to acquire LTE frames and determine the cell identity for extracting the received CRS and generating the local CRS, respectively. After that, frequency-domain correlation is used to estimate the channel frequency response which can be subsequently transformed to the CIR by the inverse fast Fourier transform operation [*Zhou et al*., 2013].

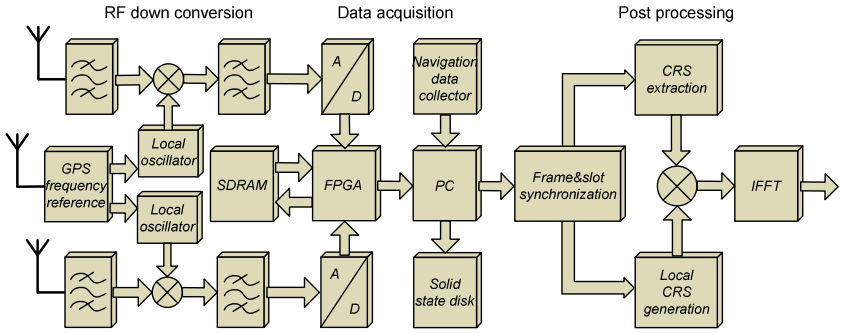

Figure 2. Block diagram of LTE sounder.

2.2. Measurement Campaign

It is reported that the LTE networks have almost covered all HSRs in China, for a total of 15,000 km by 2014. Choosing one eNB in the LTE network on Beijing to Tianjin HSR, the measurement campaign in a station scenario is taken based on the proposed system, as shown in Figure 3. At the eNB side, the CRSs are transmitted by a ±45° cross-polarized directional antenna at 1890 MHz frequency and 18 MHz bandwidth with 12.2 dBm transmitted power, 17.4 dBi gain, 67° horizontal beam width, and 6.6° vertical beam width. The eNB has 30 m height and approximates 30 m away from the track. At the receiver side, the LTE sounder, built by a GPS discipline clock, two RF units, a dual-channel data acquisition card, a SSD, and a PC, is employed. Automatic gain control of the RF unit is disabled, and the attenuation of the RF units is fixed to 25 dB. As shown in Figure 3, train-mounted antennas (antennas 5 and 6 marked with red circles), HUBER + SUHNER [*HUBER+SUHNERAG RF Industrial*, 2010], with the spacing of 1.2 m or 7.6 wavelengths and 8.5 dBi gain are used for the multiantenna relay-helped measurement. Antenna 1 is utilized to receive the GPS signal, whereas antenna 3 is connected to the spectrum analyzer to monitor the signal state. Note that antennas 2 and 4 which can only be available for the specific GSM-R network are unused.

The high-speed test train (CRH380B-002) with 285 km/h averaged mobility velocity, 200 m length, 4 m height, and 3 m width is running through the station under a viaduct with 10 m height from Tianjin to Beijing. The measured scenario can be regarded as the open-type station in which the awnings only cover the platform supporting a clear free space over the rail [*Guan et al.*, 2014]. However, the awnings can still produce lots of scattering and reflecting waves to complicate the fading behavior. The width and height of the awning is 15 m and 10 m, respectively, and the width of the gap between the awnings is 20 m. The measurement route can be classified into three segments: Region A, Region B, and Region C. In Region A the station has almost no impact on the channel, whereas in Regions B and C the propagation condition suffers from the direct and indirect effects of the station. This paper mainly focuses on the overall channel characteristics in Regions B and C.

2.3. Measurement Data

After the postprocessing, the raw CIRs covering 1260 m distance are acquired, which can be denoted by $h_{i,j}(n,\tau)$ where n is the snapshot index, τ is the multipath tap index, and i and j are the indices of the antenna elements at the eNB and the receiver sides, respectively. To extract the large-scale data, the reference signal received power (RSRP) that can be calculated by taking the sum of the CIR power versus time delay is averaged by a sliding window with the length of W according to

$$P_{i,j}^{\mathrm{LS}}(n) = \frac{1}{W}\sum_{k=n}^{k+W-1} \int \left|h_{i,j}(k,\tau)\right|^2 \mathrm{d}\tau, \tag{1}$$

where W is commonly chosen to be 20 wavelengths in the mobile measurement [*Zhao et al.*, 2002], corresponding to the distance of 3.17 m at 1.89 GHz. Removing the large-scale fading effect from the CIRs, the small-scale data with wideband and narrowband forms can be respectively obtained as follows:

$$h_{i,j}^{\mathrm{SS}}(n,\tau) = h_{i,j}(n,\tau)/\sqrt{P_{i,j}^{\mathrm{LS}}(n)} \tag{2}$$

and

$$h_{i,j}^{\mathrm{SS}}(n) = \int h_{i,j}^{\mathrm{SS}}(n,\tau)\mathrm{d}\tau. \tag{3}$$

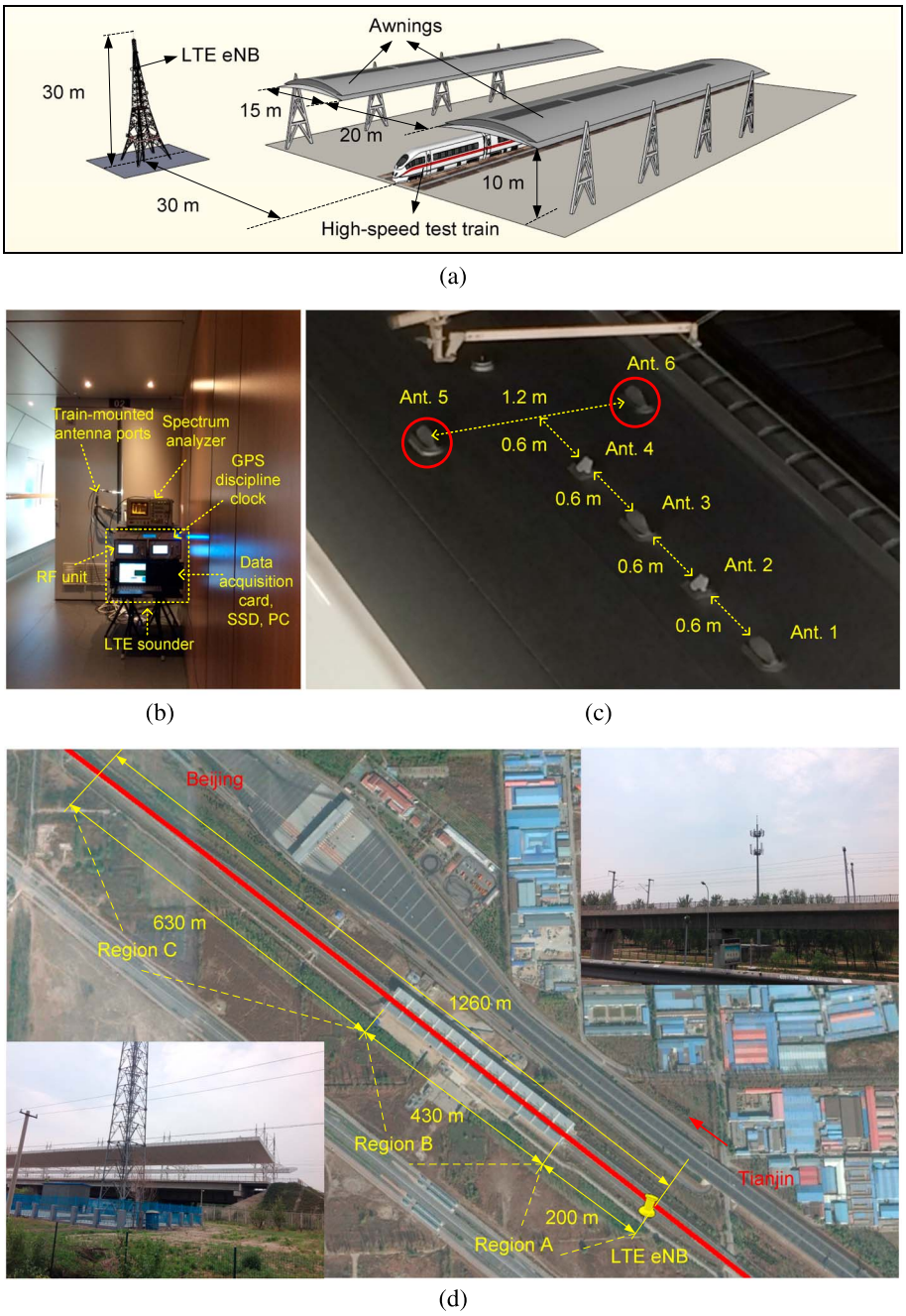

Figure 3. LTE-based channel measurement. (a) Measurement scenario. (b) Measurement equipment. (c) Structure of train-mounted antennas. (d) Measurement route and environment.

Figure 4 plots the extracted large-scale data and narrowband small-scale data. It is observed that when the distance between the eNB and the receiver is less than 120 m, the RSRP is relatively weak and experiences an upward trend. This is because the train is underneath the eNB antenna, and the receiver is not in the main-lobe of the antenna pattern of the directional antenna [*He et al.*, 2013b]. However, when the train is moving away from the bottom of the eNB, the RSRP starts to decrease gradually with the distance. Since this paper only considers the channel characteristics in the station-related region, the large-scale and small-scale data within 1060 m distance from 200 m to 1260 m are used for the analysis.

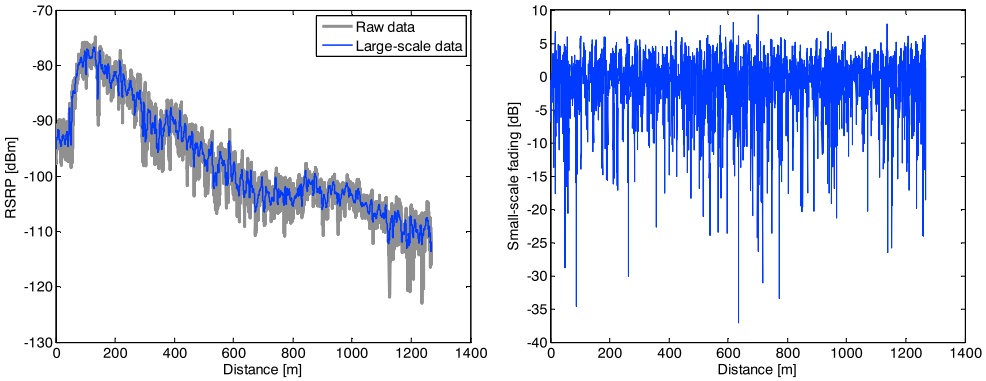

Figure 4. Large-scale and narrowband small-scale data.

3. Large-Scale Characteristics

Large-scale characteristics can make the network deployment and the network optimization reliable and efficient, so as to enhance the performance of wireless networks. In this section, based on the extracted large-scale data, PL and SF will be analyzed.

3.1. Path Loss

PL as one of important large-scale parameters can help to predict the signal attenuation, which is defined as the decibel (dB) value of the ratio of the transmitted power to the received power. Denoting the transmitted power of CRS, transmit antenna gain, receive antenna gain, RF attenuation as P_T, G_T, G_R, and A_{RF}, respectively, the PL is calculated as follows:

$$P_L(\mathrm{dB}) = P_T(\mathrm{dBm}) + G_T(\mathrm{dBi}) + G_R(\mathrm{dBi}) - P_{1,1}^{\mathrm{LS}}(\mathrm{dBm}) - A_{\mathrm{RF}}(\mathrm{dB}). \tag{4}$$

The PL is conventionally modeled as a function of logarithmic distance. The empirical PL model is given by *Liu et al.* [2012]:

$$P_L(d) = a + 10n\cdot\log_{10}d, \tag{5}$$

where a stands for the intercept, d is the distance between the transmitter and the receiver in meters, and n indicates the PL exponent.

Figure 5 shows the measured PL result and the PL model in the station scenario and compares the proposed PL model with free space model, WINNER II D2a model [*Kyösti et al.*, 2007], and PL results in open viaduct [*Liu et al.*, 2012], obstructed viaduct [*Guo et al.*, 2012], cutting [*Sun et al.*, 2013], and hilly terrain [*Luan et al.*, 2013] environments. The fitting parameters a and n of the PL model are found to be 19.5 and 3.32, respectively. Due to the effect of the train carriage roof, the PL exponent of station has much higher value than that of free space model. This phenomenon is also observed in WINNER D2a model. The PL exponent in the station scenario is larger than the values of 3.03 and 2.83 in the open viaduct and cutting environments but is smaller than the value of 3.56 in the obstructed viaduct environment where there are more scatterers such as dense trees. Moreover, the PL exponent for station is higher than the value of 2.4 for hilly terrain in short distance but is lower than that of 3.88 in over 788.6 m distance.

3.2. Shadow Fading

The SF is caused by obstruction in the propagation path between the transmitter and the receiver, which describes the signal power variation related to the change in the environment that is experienced at a slow rate. In the design of diversity and handover schemes a better understanding of the standard deviation and the autocorrelation property of SF is critical. The SF can be obtained by subtracting the established PL model from the measured PL data. In most literatures, the SF in decibels is characterized by a zero-mean random variable following the log-normal distribution as follows:

$$X_{\mathrm{SF}} \sim N\left(0, \sigma_{\mathrm{SF}}^2\right), \tag{6}$$

where σ_{SF} denotes the standard deviation of SF.

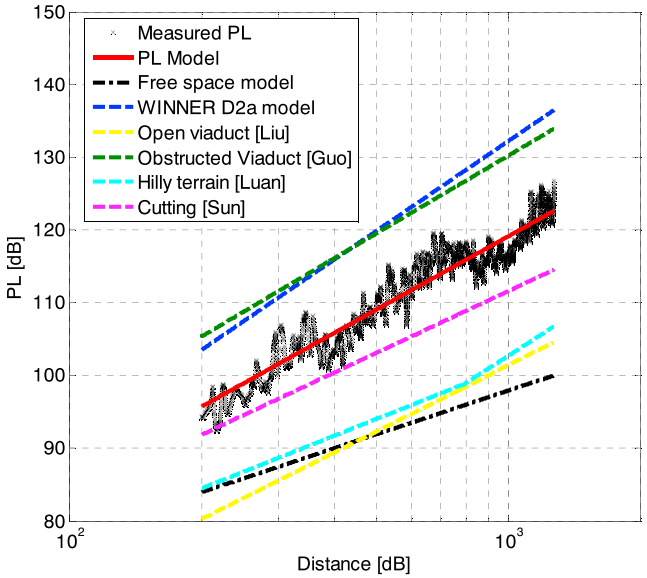

Figure 5. Path loss results in the measured station scenario and in other scenarios of previous literatures.

The autocorrelation of SF indicates the correlation of SF among the same radio link in different locations, defined as follows:

$$\rho_{\mathrm{SF}}(\Delta d) = \frac{E\{X_{\mathrm{SF}}(d)X_{\mathrm{SF}}(d+\Delta d)\}}{\sigma_{\mathrm{SF}}(d)\sigma_{\mathrm{SF}}(d+\Delta d)}, \quad (7)$$

where $E\{\cdot\}$ denotes the expected value of $\{\cdot\}$ and Δd represents the separation distance of two locations. The autocorrelation of SF is commonly modeled by the single exponential decay function [*Gudmundson*, 1991] as

$$\rho_{\mathrm{SF}}(\Delta d) = e^{-\frac{\Delta d}{d_S}}, \quad (8)$$

where d_S indicates the decorrelation distance, which reflects how fast the large-scale characteristics are changing over the distance and is dependent on the environment. The decorrelation distance is taken for the normalized autocorrelation to fall to 0.37 (e^{-1}). Alternatively, the double exponential decay function [*Szyszkowicz et al.*, 2010] is also widely used as follows:

$$\rho_{SF}(\Delta d) = \alpha e^{-\frac{\Delta d}{d_1}} + (1-\alpha)e^{-\frac{\Delta d}{d_2}} \quad (9)$$

where $0 \le \alpha \le 1$, d_1, and d_2 are the tunable parameters.

Figure 6 illustrates the statistical characteristic of SF, focusing on probability density function (PDF). It is found that the measured SF data fits the normal distribution well with $\sigma_{\mathrm{SF}} = 2.21$ dB. In the case of the same length of the sliding window for extracting large-scale data, the σ_{SF} in the station scenario is larger than the values of 2.0 dB and 1.66 dB in the open viaduct and cutting environments [*Liu et al.*, 2012; *Sun et al.*, 2013]. Due to the different sliding window lengths, the comparison of SF with other scenarios is not considered here.

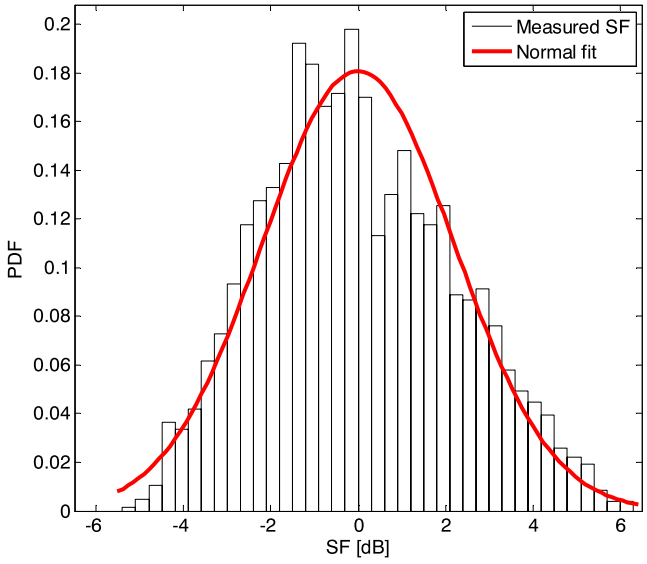

Figure 6. PDF of shadow fading in the station scenario.

Figure 7 depicts the autocorrelation coefficient of SF for the measurement and model results. It is found that the double exponential decay model provides a better match to the measured autocorrelation function. The fitting parameters of the single and double exponential decay functions are $d_S = 29.3$ m, $\alpha = 0.46$, $d_1 = 4.1$ m, and $d_2 = 65.6$ m. The decorrelation distance in the station scenario is larger than the value of 10.3 m measured in the hilly terrain environment [*Luan et al.*, 2013] but is smaller than the value of about 40 m for line of sight (LOS) scenario of RMa in M. 2135 [*International Telecommunication Union-Recommendation*, 2008]. This implies that the variation of the large-scale parameters in the station scenario is faster than the hilly terrain environment but slower than the LOS scenario

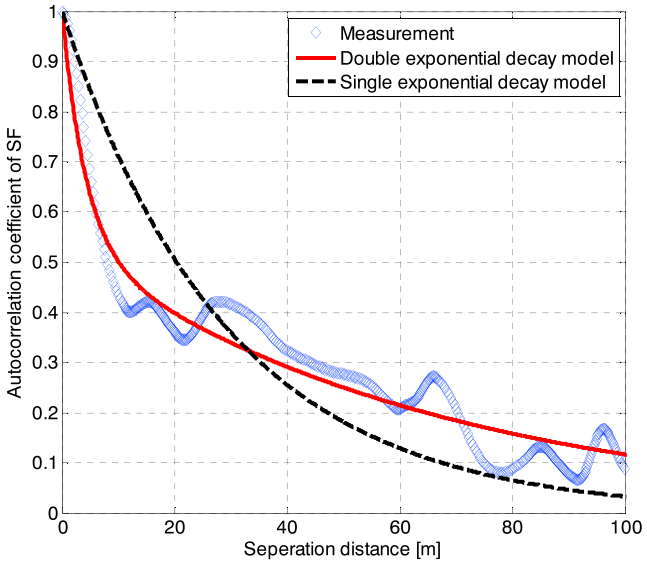

Figure 7. Autocorrelation coefficient of shadow fading in the station scenario.

of RMa. In particular, the measured decorrelation distance is lower than all the 930 MHz GSM-R measurement results in *He et al.* [2014].

4. Small-Scale Characteristics

Small-scale characteristics are useful for physical layer design, as it helps engineers design countermeasures to small-scale fading, such as diversity transmission/reception, error correction coding and interleaving, and equalization algorithms. In this section, three typical small-scale parameters in the station scenario, involving K-factor, root-mean-square (RMS) DS, and SC, will be discussed.

4.1. Ricean K-Factor

The K-factor measures how much local fading the signal undergoes over space, which is defined as the power ratio of line of sight (LOS) components to nonline of sight (NLOS) components in the received signal. Based on the narrowband small-scale data, using a moment-based method [*Greenstein et al.*, 1999], the K-factor is estimated in the same set of 10 m windows as follows:

$$K(n)=\frac{\sqrt{1-\frac{\mathrm{Var}\left\{\left|h_{1,1}^{SS}(n)\right|^2\right\}}{E^2\left\{\left|h_{1,1}^{SS}(n)\right|^2\right\}}}}{1-\sqrt{1-\frac{\mathrm{Var}\left\{\left|h_{1,1}^{SS}(n)\right|^2\right\}}{E^2\left\{\left|h_{1,1}^{SS}(n)\right|^2\right\}}}}, \tag{10}$$

where Var{·} denotes the variance of {·}.

A distance-dependent statistical model [*Zhou et al.*, 2014b] can be used to fit the K-factor data, as follows:

$$K(d)=K_{\mathrm{med}}(d)+X_K \tag{11}$$

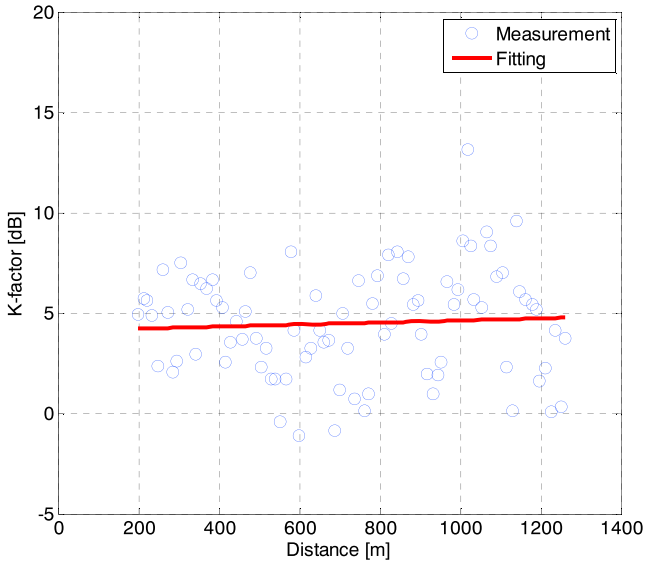

Figure 8. The narrowband K-factor against distance.

where $K_{\mathrm{med}}(d)$ indicates the median value of the K-factor and X_K represents a zero-mean Gaussian random variable with the standard deviation of σ_K. $K_{\mathrm{med}}(d)$ is usually modeled by a linear polynomial function as follows:

$$K_{\mathrm{med}}(d)=a_k+b_k d \tag{12}$$

where a_k and b_k are the parameters of the model.

In Figure 8, the estimated K-factor is plotted as a function of distance. It is observed that the variation of the K-factor almost remains stable with the increase of distance. The fitting parameters of the linear polynomial function, a_k and b_k, are found to be 4.11 dB and 0.0005, respectively. The median value of the K-factor is consistent with the result in the far zones of open station scenario

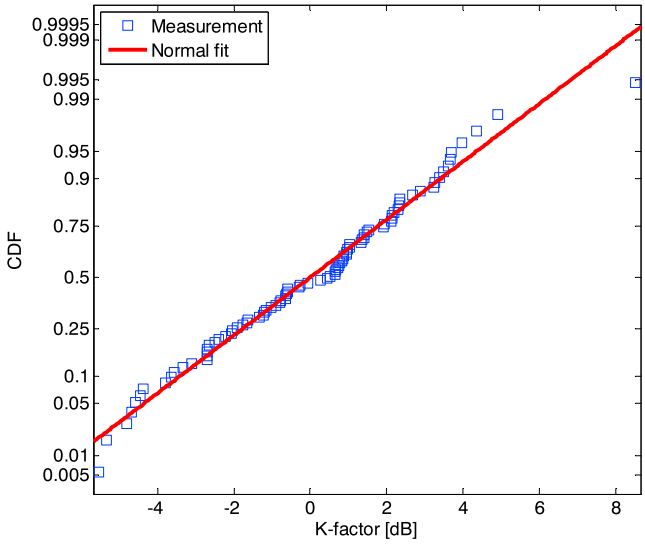

Figure 9. CDF of the narrowband K-factor about median value.

in *Guan et al.* [2014]. Moreover, compared with the result in the viaduct scenario [*Zhou et al.*, 2014a], the median value of the K-factor is lower than that in the unobstructed region (Segments A and E) but is higher than that in the obstructed area (Segments B and D). This means that the scattering components caused by the awnings would affect the strength of the K-factor. However, they have the weaker impact on the K-factor than the NLOS components produced by the high dense trees.

In order to acquire σ_K, the K-factor data are normalized by the median value and then the cumulative distribution function (CDF) of the median-normalized K-factor on a probability scale is shown in Figure 9. It is known that the closeness to a straight line on this scale implies a normal distribution. Thus, the corresponding standard deviation is 2.65 dB in the model.

4.2. Delay Spread

The mean squared magnitude of the CIR, also known as the power delay profile (PDP), is

$$\mathrm{PDP}_{i,j}(n,\tau) = \frac{1}{M}\sum_{m=1}^{M}\left|h_{i,j}^{\mathrm{SS}}(n_m,\tau)\right|^2 \tag{13}$$

where M denotes the averaged length, which are chosen to be 20 wavelengths for meeting the requirement of wide-sense stationary (WSS). This will be validated in section 5 that the length of 20 wavelengths is within the stationary region in the measured station scenario. The root-mean-square (RMS) DS is calculated by the second central moment of the PDP [*Molisch and Steinbauer*, 1999] as follows:

$$\tau_{\mathrm{RMS}}(n) = \sqrt{\frac{\int_{-\infty}^{\infty}\mathrm{PDP}_{1,1}(n,\tau)\tau^2\mathrm{d}\tau}{\int_{-\infty}^{\infty}\mathrm{PDP}_{1,1}(n,\tau)\mathrm{d}\tau} - \left(\frac{\int_{-\infty}^{\infty}\mathrm{PDP}_{1,1}(n,\tau)\tau\mathrm{d}\tau}{\int_{-\infty}^{\infty}\mathrm{PDP}_{1,1}(n,\tau)\mathrm{d}\tau}\right)^2} \tag{14}$$

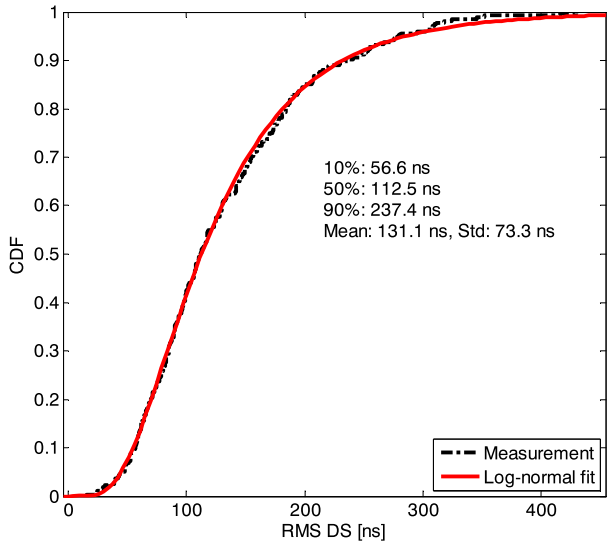

Figure 10. CDF of the RMS delay spread in the station scenario.

The model relating RMS DS to PL has been proposed in *Salous and Gokalp* [2007], expressed as follows:

$$\tau_{\mathrm{RMS}}(\mathrm{ns}) = e^{a_\tau + b_\tau P_L(\mathrm{dB})} \tag{15}$$

where a_τ and b_τ are the parameters of the model.

Figure 10 shows the CDF of the RMS DS and the fitting of the CDF with a lognormal distribution in the station scenario. The fitting parameters $\mu(\log 10(\mathrm{s}))$ and $\sigma(\log 10(\mathrm{s}))$ of the RMS DS are -6.95 and 0.24. It can be found that the RMS DS measured in the station scenario is much higher than that with the mean value of -7.4 and the standard deviation of 0.2 in the WINNER D2a model, whereas it is lower than the values in the obstructed viaduct and hilly terrain

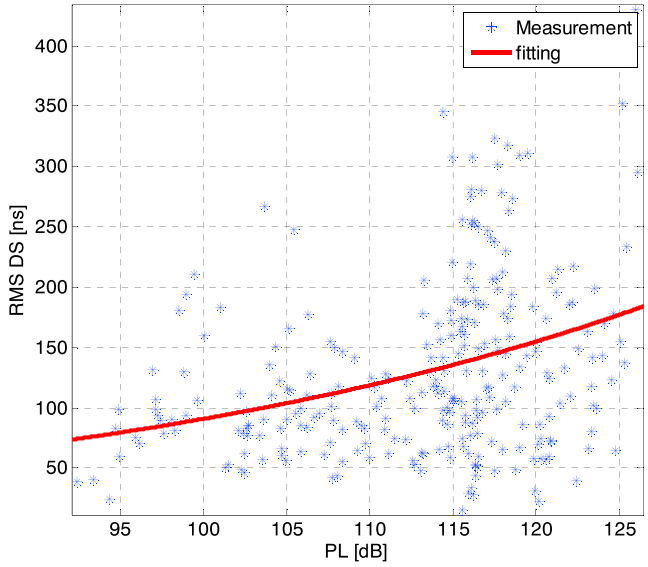

Figure 11. The RMS delay spread against PL.

scenarios reported in *Guo et al.* [2012] and *Luan et al.* [2013].

The relation between the RMS DS and the PL is illustrated in Figure 11. It is noted that the RMS DS increases exponentially with the PL from 92 to 126 dB. The reason why the RMS DS increases with the PL is that as the LOS component becomes weaker, multipath components with larger time delays and weaker power levels can be detected [*Feuerstein et al.*, 1994]. Due to the limited dynamic range of the measurement system, these weak multipath components cannot be detected when a strong direct path signal is present. The model parameters are found to be $a_\tau = 1.84$ and $b_\tau = 0.027$.

4.3. Spatial Correlation

The multiple input multiple output (MIMO) performance is dependent on the spatial correlation (SC) between the different antenna elements at both ends of the individual link. The correlation coefficient of two subchannels in the data analysis is calculated by the following:

$$\rho_{SC}(n) = \frac{E\left\{h_{1,1}^{SS}(n)\left(h_{2,2}^{SS}(n)\right)^*\right\}}{\sqrt{Var\left\{h_{1,1}^{SS}(n)\right\}Var\left\{h_{2,2}^{SS}(n)\right\}}} \tag{16}$$

where $(\cdot)^*$ denotes the complex conjugation.

Figure 12 depicts the CDF of the SC and the fitting of the CDF with a normal distribution in the station scenario. The mean value and standard deviation of the correlation coefficient are 0.55 and 0.18, respectively. It can be also seen that almost 90% of the SC values are less than 0.8. The relatively weak correlation is due to the cross-polarized antenna configuration at the BS side and the large antenna spacing at the train side. Besides, the scattering and reflecting components caused by the awnings degrade the correlation between two links as well. Thus, the MIMO technology is possible to have a good performance in the station scenario.

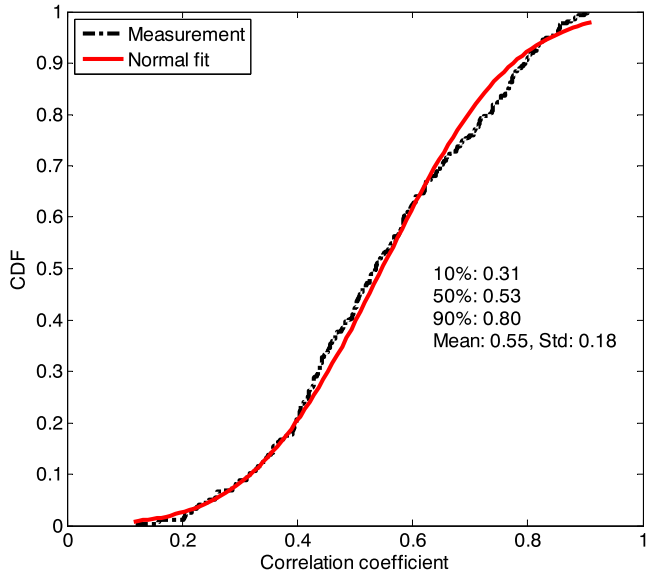

Figure 12. CDF of the spatial correlation in the station scenario.

5. Characterization of Stationary Region

High mobility leads to the violation of WSS condition for wireless channel under HSR scenarios. Nonstationary channel is a very interesting issue with great value for the selection of physical layer technologies such as synchronization, channel estimation, and equalization [*Ai et al.*, 2014].

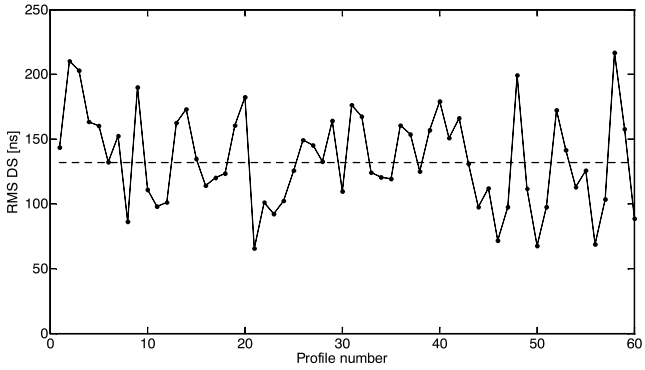

Figure 13. RMS delay spread variation about the median in the station scenario.

To test the WSS for the channel, a statistical test called the RUN test can be applied to the RMS DS data [*Salous*, 2013]. The RMS DS data are divided into N_i equal intervals where the data in each interval is considered independent. The mean and variance in each interval are then evaluated separately. The variance values are tested for an underlying trend by taking their median value and finding the values that fall above and below the median where the value is indicated by N_+ or N_- if it falls above or below the median value, respectively. The number of RUNs is equal to the following:

$$N_{\text{runs}} = N_+ + N_-. \tag{17}$$

Subsequently, half the number of RUNs is entered into the table in *Bendat and Peirsol* [1966] to identify the acceptable low and high number of RUNs for low and high confidence levels, c_{low} and c_{high}, respectively. If the number of computed RUNs falls outside these limits, as given in the following equation, then the hypothesis that the process is WSS is rejected; that is,

$$\text{check} \quad \text{if} \quad \left[c_{\text{low}} \le N_{\text{runs}} \le c_{\text{high}} | N_i\right]. \tag{18}$$

Considering $N_i = 60$ (corresponding to about 12 m distance), the RMS DS variation about the median is shown in Figure 13. The median of the RMS DS is computed as 131.7 ns and 22 RUNs is found. For confidence levels of 0.05 and 0.95, with $N_i = 60$, the acceptable RUN value is between 24 and 38. Since the number of RUNs is outside this limit, the data are considered nonstationary over the 12 m interval. To identify the stationary distance, different numbers of sections should be considered until the RUN test gives the stationary interval. Figure 14 illustrates the probability that the RUN test passes (the output of RUN test is equal to zero) when the different numbers of sections are chosen. It can be observed that in 80% of cases, the channel can be considered as stationary over a distance of around 4 m. This confirms that the WSS can be satisfied within the 20 wavelengths as mentioned in section 4.2.

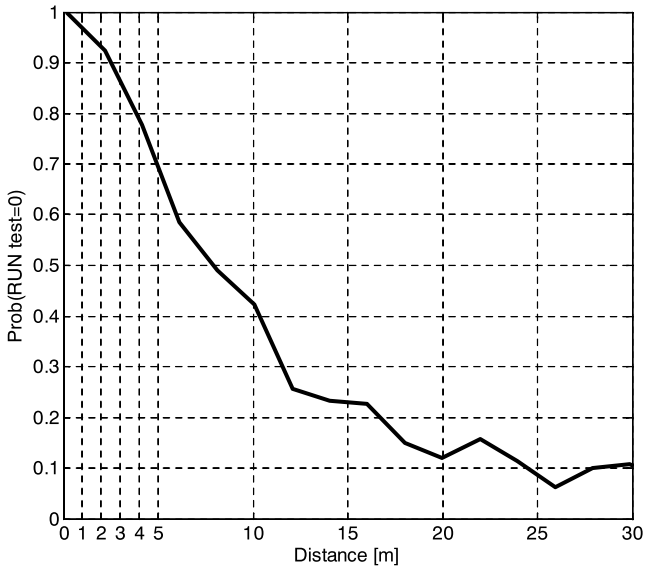

Figure 14. Probability of RUN test = 0 against distance.

6. Conclusion

This paper presents the 1.89 GHz wideband MIMO channel measurement in the HSR train station scenario in China. The LTE-based channel measurement system composed of the LTE eNB and the LTE sounder is employed to collect the time-frequency-space channel data for propagation characterization. As for the large-scale characteristics, the PL exponent and the standard deviation of SF are 3.32 and 2.21 dB, respectively. The autocorrelation property of SF is characterized by the double exponential decay model and the decorrelation distance corresponds to 29.3 m. With regard to the small-scale characteristics, the distance-dependent K-factor model and the PL-dependent RMS DS model are proposed. It is also shown that the mean value of the SC is 0.55, and almost 90%

of the values are below 0.8. In addition, applying the RUN test to the RMS DS data, the stationary interval is found to be around 4 m in 80% of cases. The measured results show the realistic channel characteristics in the HSR station scenario, which will be helpful for the design of the next-generation HSR communication system.

Acknowledgments
The authors would like to thank Huisheng Wang and Yuzheng Zhang from China Academy of Railway Sciences for their help to perform the channel measurements and Long Sun from Huawei for the useful discussion of LTE railway network structure and configuration. The research was supported in part by the NSFC projects under grants 61371070 and 61471030, Beijing Natural Science Foundation (4142041 and 4152043), the open research fund of National Mobile Communications Research Laboratory, Southeast University (2014D05), and Fundamental Research Funds for the Central Universities under grant 2015JBM011. The data related to the results shown in the paper may be obtained by contacting the corresponding author.

References

Ai, B., X. Cheng, T. Kürner, Z. D. Zhong, K. Guan, R. S. He, L. Xiong, D. W. Matolak, D. G. Michelson, and C. B. Rodriguez (2014), Challenges toward wireless communications for high-speed railway, *IEEE Trans. Intell. Transp.*, *15*(5), 2143–2158.

Bendat, J. S., and A. G. Peirsol (1966), *Measurements and Analysis of Random Data*, pp. 396, John Wiley, Hoboken, N. J.

Briso, C., J. M. Cruz, and J. I. Alonso (2007), Measurements and modeling of distributed antenna systems in railway tunnels, *IEEE Trans. Veh. Technol.*, *56*(5), 2870–2879.

Calle-Sanchez, J., M. Molina-Garcia, and J. I. Alonso (2012), Top challenges of LTE to become the next generation railway communication system, paper presented at 13th International Conference on Design and Operation in Railway Engineering (COMPRAIL), Wessex Institute of Technol., New Forest, U. K.

Feuerstein, M. J., K. L. Blackard, T. S. Rappaport, S. Y. Seidel, and H. H. Xia (1994), Path loss, delay spread, and outage models as functions of antenna height for microcellular system design, *IEEE Trans. Veh. Technol.*, *43*(3), 487–497.

Greenstein, L., D. Michelson, and V. Erceg (1999), Moment-method estimation of the Ricean K-factor, *IEEE Commun. Lett.*, *3*(6), 175–176.

Guan, K., Z. D. Zhong, B. Ai, and T. Kürner (2014), Propagation measurements and analysis for train stations of high-speed railway at 930 MHz, *IEEE Trans. Veh. Technol.*, *63*(8), 3499–3516.

Gudmundson, M. (1991), Correlation model for shadow fading in mobile radio systems, *Electron. Lett.*, *27*(23), 2145–2146.

Guo, Y., J. Zhang, C. Tao, L. Liu, and L. Tian (2012), Propagation characteristics of wideband high-speed railway channel in viaduct scenario at 2.35 GHz, *J. Modern Transp.*, *20*(4), 206–212, doi:10.1007/BF03325800.

He, R. S., Z. D. Zhong, B. Ai, and J. Ding (2011a), An empirical path loss model and fading analysis for high-speed railway viaduct scenarios, *IEEE Antennas Wireless Propag Lett.*, *10*, 808–812.

He, R. S., Z. D. Zhong, B. Ai, and J. Ding (2011b), Propagation measurements and analysis for high-speed railway cutting scenario, *Electron. Lett.*, *47*(21), 1167–1168.

He, R. S., Z. D. Zhong, B. Ai, J. Ding, Y. Yang, and A. F. Molisch (2013a), Short-term fading behavior in high-speed railway cutting scenario: Measurements, analysis, and statistical models, *IEEE Trans. Antennas Propag.*, *61*(4), 2209–2222.

He, R. S., Z. D. Zhong, B. Ai, G. Wang, J. Ding, and A. F. Molisch (2013b), Measurements and analysis of propagation channels in high-speed railway viaducts, *IEEE Trans. Wireless Commun.*, *12*(2), 794–805.

He, R. S., Z. D. Zhong, B. Ai, and C. Oestges (2014), Shadow fading correlation in high-speed railway environments, *IEEE Trans. Veh. Technol.*, *64*(7), 2762–2772.

HUBER + SUHNERAG RF Industrial (2010), Sencity Rail Antenna: 1399.17.0039 HUBER + SUHNER datasheet. [Available at http://www.hubersuhner.com/ProdDet/4693746.]

International Telecommunication Union-Recommendation (2008), Guidelines for evaluation of radio interface technologies for IMT-Advanced, Rep. ITU-R M.2135.

Kyösti, P., et al. (2007), WINNER II channel models, IST-WINNER II D1.1.2.

Liu, L., C. Tao, J. H. Qiu, H. J. Chen, L. Yu, W. H. Dong, and Y. Yuan (2012), Position-based modeling for wireless channel on high-speed railway under a viaduct at 2.35 GHz, *IEEE J. Sel. Areas Commun.*, *30*(4), 834–845.

Liu, L., C. Tao, R. Sun, H. Chen, and Z. Lin (2014), Non-stationary channel characterization for high-speed railway under viaduct scenarios, *Chin. Sci. Bull.*, *59*(35), 4988–4998.

Luan, F. Y., Y. Zhang, L. M. Xiao, C. H. Zhou, and S. D. Zhou (2013), Fading characteristics of wireless channel on high-speed railway in hilly terrain scenario, *Int. J. Antennas Propag*, *2013*, 378407, doi:10.1155/2013/378407.

Matolak, D. W. (2014), Modeling the vehicle-to-vehicle propagation channel: A review, *Radio Sci.*, *49*, 721–736, doi:10.1002/2013RS005363.

Molisch, F., and M. Steinbauer (1999), Condensed parameters for characterizing wideband mobile radio channels, *Int. J. Wireless Inf. Networks*, *6*(3), 133–154.

Razavi-Ghods, N., and S. Salous (2009), Wideband MIMO channel characterization in TV studios and inside buildings in the 2.2–2.5 GHz frequency band, *Radio Sci.*, *44*, RS5015, doi:10.1029/2008RS004095.

Renaudin, O., V. Kolmonen, P. Vainikainen, and C. Oestges (2010), Non-stationary narrowband MIMO inter-vehicle channel characterization in the 5-GHz band, *IEEE Trans. Veh. Technol.*, *59*(4), 2007–2015.

Salous, S. (2013), *Radio Propagation Measurement and Channel Modelling*, pp. 280–285, John Wiley, West Sussex, U. K.

Salous, S., and H. Gokalp (2007), Medium- and large-scale characterization of UMTS-allocated frequency division duplex channels, *IEEE Trans. Veh. Technol.*, *56*(5), 2831–2843.

Sun, R. C., C. Tao, L. Liu, and Z. H. Tan (2013), Channel measurement and characterization for HSR U-shape groove scenarios at 2.35 GHz, paper presented at 78th Vehicular Technology Conference (VTC Spring), IEEE Vehicular Technol. Soc., Las Vegas, Nev.

Szyszkowicz, S. S., H. Yanikomeroglu, and J. S. Thompson (2010), On the feasibility of wireless shadowing correlation models, *IEEE Trans. Veh. Technol.*, *59*(9), 4222–4236.

Zhang, J. Y., Z. H. Tan, Z. D. Zhong, and Y. Kong (2010), A multi-mode multi-band and multi-system-based access architecture for high-speed railways, paper presented at 72nd Vehicular Technology Conference (VTC Fall), IEEE Vehicular Technol. Soc., Ottawa, Canada.

Zhang, Y., Z. W. He, W. C. Zhang, L. M. Xiao, and S. D. Zhou (2014), Measurement-based delay and Doppler characterizations for high-speed railway hilly scenario, *Int. J. Antennas Propag*, *2014*, 875345, doi:10.1155/2014/875345.

Zhao, X., J. Kivinen, P. Vainikainen, and K. Skog (2002), Propagation characteristics for wideband outdoor mobile communications at 5.3 GHz, *IEEE J. Sel. Areas Commun.*, *20*(3), 507–514.

Zhou, T., C. Tao, L. Liu, and Z. H. Tan (2013), A study on a LTE-based channel sounding scheme for high-speed railway scenarios, paper presented at 78th Vehicular Technology Conference (VTC Spring), IEEE Vehicular Technol. Soc., Las Vegas, Nev.

Zhou, T., C. Tao, L. Liu, and Z. Tan (2014a), A semiempirical MIMO channel model in obstructed viaduct scenarios on high-speed railway, *Int. J. Antennas Propag*, *2014*, 287159, doi:10.1155/2014/287159.

Zhou, T., C. Tao, L. Liu, and Z. H. Tan (2014b), Ricean K-factor measurements and analysis for wideband high-speed railway channels at 2.35 GHz, *Radioengineering*, *23*(2), 578–585.

Zhou, T., C. Tao, S. Salous, L. Liu, and Z. H. Tan (2015), Channel sounding for high-speed railway communication systems, *IEEE Commun. Mag.*, *53*(10), 70–77.